ORIGINAL ARTICLE

Gold nanoparticle-directed autophagy intervention for antitumor immunotherapy *via* inhibiting tumor-associated macrophage M2 polarization

Siyue Zhang[a,b,c,f,†], Fangyuan Xie[a,d,†], Kaichun Li[e,†], He Zhang[a,†], You Yin[i,†], Yuan Yu[a], Guangzhao Lu[a], Shihao Zhang[g], Yan Wei[c], Ke Xu[c], Yan Wu[j], Hong Jin[k], Lan Xiao[l], Leilei Bao[d], Can Xu[h,*], Yulin Li[g,m,*], Ying Lu[a,*], Jie Gao[b,c,*]

[a]*Department of Pharmacy, Naval Medical University, Shanghai 200433, China*
[b]*Changhai Clinical Research Unit, Shanghai Changhai Hospital, Naval Medical University, Shanghai 200433, China*
[c]*Institute of Translational Medicine, Shanghai University, Shanghai 200444, China*
[d]*Department of Pharmacy, Shanghai Eastern Hepatobiliary Surgery Hospital, Naval Medical University, Shanghai 200433, China*
[e]*Department of Oncology, Shanghai Fourth People's Hospital, School of Medicine, Tongji University, Shanghai 200434, China*
[f]*Unit for Drug and Instrument Supervision and Inspection of Wuxi Joint Logistic Support Center, Nanjing 210000, China*
[g]*Key Laboratory for Ultrafine Materials of Ministry of Education, Engineering Research Center for Biomedical Materials of Ministry of Education, School of Materials Science and Engineering, East China University of Science and Technology, Shanghai 200237, China*
[h]*Department of Gastroenterology, Shanghai Changhai Hospital, Naval Medical University, Shanghai 200433, China*
[i]*Department of Neurology, Changzheng Hospital, Naval Medical University, Shanghai 200003, China*
[j]*Department of Biomaterial, College of Life Sciences, Mudanjiang Medical University, Mudanjiang 157011, China*
[k]*Department of Laboratory Medicine, Hongqi Hospital, Mudanjiang Medical College, Mudanjiang 157011, China*
[l]*Centre for Biomedical Technologies, Queensland University of Technology, Brisbane QLD 4000, Australia*
[m]*Wenzhou Institute of Shanghai University, Wenzhou 325000, China*

*Corresponding authors. Tel./fax: +86 21 31166666, +86 21 81871290, +86 21 64252763.
E-mail addresses: xucan@smmu.edu.cn (Can Xu), yulinli@ecust.edu.cn (Yulin Li), acuace@163.com (Ying Lu), jmsx2021@shu.edu.cn (Jie Gao).
†These authors made equal contributions to this work.

Abstract   Tumor-associated macrophages (TAMs), one of the dominating constituents of tumor micro-environment, are important contributors to cancer progression and treatment resistance. Therefore, regulation of TAMs polarization from M2 phenotype towards M1 phenotype has emerged as a new strategy for tumor immunotherapy. Herein, we successfully initiated antitumor immunotherapy by inhibiting TAMs M2 polarization *via* autophagy intervention with polyethylene glycol-conjugated gold nanoparticles (PEG-AuNPs). PEG-AuNPs suppressed TAMs M2 polarization in both *in vitro* and *in vivo* models, elicited antitumor immunotherapy and inhibited subcutaneous tumor growth in mice. As demonstrated by the mRFP-GFP-LC3 assay and analyzing the autophagy-related proteins (LC3, beclin1 and P62), PEG-AuNPs induced autophagic flux inhibition in TAMs, which is attributed to the PEG-AuNPs induced lysosome alkalization and membrane permeabilization. Besides, TAMs were prone to polarize towards M2 phenotype following autophagy activation, whereas inhibition of autophagic flux could reduce the M2 polarization of TAMs. Our results revealed a mechanism underlying PEG-AuNPs induced antitumor immunotherapy, where PEG-AuNPs reduce TAMs M2 polarization *via* induction of lysosome dysfunction and autophagic flux inhibition. This study elucidated the biological effects of nanomaterials on TAMs polarization and provided insight into harnessing the intrinsic immunomodulation capacity of nanomaterials for effective cancer treatment.

1. Introduction

Tumor microenvironment promotes tumorigenesis, metastasis, and drug resistance of tumors[1,2]. Tumor-associated macrophages (TAMs) is a dominating constituent in tumor microenvironment and a vital target for cancer therapy[3-5]. Macrophages are immune cells which polarize towards different directions under certain stimuli, and the two extremes of the polarization of macrophages are defined as M1 and M2 phenotypes, respectively. Most TAMs show a typical M2 phenotype characterized by high expression of immunosuppressive factors, *e.g.*, transforming growth factor-beta (TGF-β), interleukin-10 (IL-10), vascular endothelial growth factor (VEGF)], which could significantly promote tumor progression. Accordingly, inhibition of the M2 polarization has been reported to induce potent antitumor effects[6,7]. For instance, it has been reported that all-*trans* retinoic acid (ATRA) inhibited the initiation and stemness of osteosarcoma by preventing the M2 polarization of TAMs[8], while ovatodiolide was shown to reduce TAMs M2 polarization and colon tumorigenesis through yes-associated protein 1 (YAP1) oncogenic pathways[9]. Therefore, regulation of TAMs polarization has emerged as a new strategy for tumor immunotherapy.

Recent advances in nanomaterials have shown that nanomaterials are potential candidates for TAM immunomodulation. The intrinsic biological effects of nanomaterials have attracted a lot of attention recently because of their unique and tunable physicochemical properties[10,11]. It has been demonstrated that nanomaterials administered systemically or locally are readily internalized by TAMs, and thus nanomaterials have been extensively investigated in targeting TAMs in cancer diagnostic and therapy[12-14]. Therefore, it is critical to investigate the effects of nanomaterials on TAMs polarization and cancer treatment. Studies have found that inorganic nanomaterials like gold nanoparticles (AuNPs) are more likely to be internalized by M2 macrophages[15,16]. Further, noble metal nanomaterials-induced oxidative stress can reprogram TAMs from the M2 to M1 phenotype[17].

Nevertheless, the intrinsic mechanisms underlying nanomaterials on TAMs polarization are not well understood.

Autophagy is a conserved cellular catabolic pathway, which is characterized by the formation of autophagosomes (a kind of double-layer membrane vesicles). Autophagy can degrade misfolded proteins, damaged or excessive organelles through the lysosome mediated pathway[18]. It has been reported that autophagy was crucial in mediating macrophage polarization[19-21]. For example, cathepsins and IL-6 have been reported to promote macrophage M2 polarization by inducing autophagy[19-21], whereas neferine was shown to induce autophagy and reduce M2 polarization of macrophages by inhibiting the mammalian target of rapamycin (mTOR)/70-kDa ribosomal protein S6 kinase (P70S6K) pathway[22]. Autophagy activation with baicin treatment can repolarize TAMs toward the M1 phenotype[23]. These data suggested autophagy modulation may serve as a functional target for regulating macrophage polarization.

Nanomaterials, defined as materials with the nanometer size range, have emerged as new autophagy modulators[24-27]. Nondegradable nanomaterials, such as iron oxide and silica nanoparticles can induce autophagy through oxidative stress. After cell entry, they destroy mitochondrial function and generate a series of reactive oxygen species[28-30]. Several reports[26,31] have suggested that nanomaterials function as autophagy activators, as reflected by the increased processing of autophagy protein such as microtubule-associated protein light chain 3 (LC3). The term "autophagic flux", used to represent the dynamic process of autophagy, is a more reliable indicator to estimate the activation or inhibition of autophagy[32]. The possibility of autophagic flux inhibition was not often investigated in nanoparticles, thus the activated autophagic flux by nanomaterials in many cases is uncertain[32]. In fact, since nanomaterials have been reported to cause damage to lysosomal ultrastructure and increase membrane permeability, many kinds of nanomaterials have been reported to inhibit autophagic flux[33]. Therefore, nanomaterials are potential tools for autophagy modulation and may induce M1 repolarization of TAMs, as well as

antitumor immunotherapy. However, to our knowledge, no studies have been undertaken to examine the effect of autophagy modulation of nanomaterials on M1 repolarization of TAMs.

In this study, we discussed the potential effect and underlying mechanism of nanomaterials, polyethylene glycol-conjugated AuNPs (PEG-AuNPs) as a model nanomaterial due to their biocompatibility as well as colloidal stability, on the polarization of TAMs. The results showed that PEG-AuNPs induced antitumor immunotherapy inhibiting TAMs M2 polarization *via* autophagy intervention. PEG-AuNPs could induce autophagic flux inhibition in TAMs, which is attributed to the induction of lysosome alkalization and membrane permeabilization by PEG-AuNPs. Besides, TAMs polarized towards the M2 phenotype following autophagy activation, whereas inhibition of autophagic flux could reduce the M2 polarization of TAMs. This study elucidated the regulatory effects of nanomaterials on TAMs polarization and provided insight into harnessing the intrinsic immunomodulation of nanomaterials for effective cancer treatment.

2.   Materials and methods

2.1.   Materials

HAuCl$_4$·4H$_2$O, citric acid, and NaBH$_4$ were bought from Sinopharm Chemical Reagent Co., Ltd. (Shanghai, China). The linear heterobifunctional PEGylation reagent, thiol polyethylene glycol amine (NH$_2$-PEG-SH) and thiol fluorescein isothiocyanate labeled polyethylene glycol (FITC-PEG-SH) were purchased from Shanghai Jinpan Co., Ltd. (Shanghai, China). The cell culture medium Dulbecco's modified Eagle medium (DMEM), fetal bovine serum (FBS), LysoSensor Green DND-189 dye, acridine orange (AO), Lipofectamine 2000 and PC7 anti-mouse CD86 antibody (*Cat. No.* 25-0862-80) were purchased from Thermo Fisher Scientific (Waltham, MA, USA). FITC-conjugated anti-mouse CD11C antibody (Cat. No. 117306), FITC-conjugated anti-mouse CD3 antibody (Cat. No. 100204), APC-conjugated anti-mouse CD4 antibody (Cat. No. 100412), and PE-labeled anti-mouse CD8 antibody (Cat. No. 162304) were purchased from BioLegend (San Diego, CA, USA). The Tunel Kit, protease K, rabbit anti-mouse KI67 antibody, and HRP conjugated goat anti-rabbit secondary antibody were purchased from Servicebio (Wuhan, China). Fresh DAB chromogenic solution was purchased from DAKO (Glostrup, Denmark). The cell culture antibiotics, penicillin/streptomycin, were obtained from Thermo Scientific HyClone (Logan, UT, USA). The Cell Counting Kit 8 (CCK-8), a Colorimetric Assay Kit used to evaluate cell proliferation and cytotoxicity, was bought from Dojindo Laboratories (Kumamoto, Japan). Percoll density gradient was obtained from Pharmacia (Uppsala, Sweden). The RNA Fast 200 Extraction Kit was bought from Fastagen Biotechnology (Shanghai, China). SYBR Premix Ex Taq™ and PrimeScript™ RT Master Mix were purchased from Takara (Otsu, Shiga, Japan). The Enzyme-Linked Immunosorbent Assay (ELISA) Kit used to perform a common immunoassay was purchased from R&D Systems Inc. (Minneapolis, MN, USA). mRFP-GFP-LC3 adenovirus used to detect the autophagy flux was purchased from Shanghai HanBio Inc. (Shanghai, China). *Atg5* siRNA were purchased from Genepharm Biotech (Shanghai, China).

2.2.   Synthesis of polyethylene glycol-conjugated gold nanoparticles (PEG-AuNPs)

The synthesis of AuNPs with diameter of 5 nm was performed by the sodium borohydride reduction approach[34]. In brief, a mixed aqueous solution of HAuCl$_4$·4H$_2$O (0.25 mmol/L) and Na$_3$C$_6$H$_5$O$_7$·2H$_2$O (0.25 mmol/L) was prepared with ultrapure water and stirred vigorously for 1 min. Then, 2 mL of a freshly prepared NaBH$_4$ solution (100 mmol/L) was added to the mixed solution and stirred for 12 h at 25 °C. The solution was centrifuged at 3500 rpm (ThermoFisher, Sorvall ST1 Plus, Shanghai, China) for 30 min with an ultrafiltration tube (MWCO 100 kDa), aiming to remove unconjugated or unreacted chemicals. Then, Na$_3$C$_6$H$_5$O$_7$·2H$_2$O solution (1.25 mmol/L) was added and the product was redissolved with ultrasound. AuNPs with diameters of 20, 50, and 100 nm were prepared by changing the concentrations of HAuCl$_4$·4H$_2$O and Na$_3$C$_6$H$_5$O$_7$·2H$_2$O.

To minimize the adsorption of serum proteins to AuNPs and maximize their stability, AuNPs of all four sizes were PEGylated. In brief, NH$_2$-PEG-SH (0.25 mmol/L, 2.4 mL) was added into 6 mL of AuNP citric acid solution and adjusted to 12 mL with Milli-Q® water. The mixed solution was stirred vigorously at 25 °C for 20 min and kept at 4 °C overnight. After centrifugation at 3500 rpm (ThermoFisher) for 30 min with an ultrafiltration tube to remove unconjugated PEG, the product was redissolved in Milli-Q® water with ultrasound. Similarly, the procedure of FITC labeled AuNPs were prepared as described using FITC-PEG-SH.

All the PEG-AuNPs were validated by transmission electron microscopy (TEM, JEM 2100; JEOL, Tokyo, Japan). TEM images were taken as described below. Briefly, PEG-AuNPs were suspended in ultrapure water and sonication for 10 min was taken to disperse PEG-AuNPs. After then, a small drop of the suspension was deposited onto a carbon-coated grid and allowed to evaporate. Then, the perfectly dried grid was monitored under the TEM at 100 kV. PEG-AuNPs were also analyzed for their size by dynamic light scattering (DLS; Zetasizer Nano ZS90; Malvern, UK), and for their ultraviolet absorption spectrum by UV−Vis absorption spectroscopy with Techcomp UV2500 UV−Vis spectrophotometer.

To investigate the stability of PEG-AuNPs under storage condition, the nanoparticles were stored in PBS solution at 25 °C. At different time points, the size of PEG-AuNPs was analyzed by DLS (Zetasizer Nano ZS90; Malvern, UK).

2.3.   Cell lines and cell culture

Hepa1-6 cells (a mouse hepatoma cell line) and RAW 264.7 cells (a mouse macrophage-like, Abelson leukemia virus-transformed cell line) were obtained from Shanghai Chinese Academy of Sciences (Shanghai, China). The cells were cultured as described as follows. Briefly, the cells were cultured in DMEM supplemented with 10% (*v/v*) FBS, 100 U/mL penicillin, and 100 μg/mL streptomycin at 37 °C in a humidified atmosphere consisting of 5% CO$_2$ and 95% air. To mimic TAMs *in vitro*, RAW264.7 cells were indirectly co-cultured with Hepa1-6 cells (TSN, tumor culture supernatant) with Transwell® plates with a pore size of 0.4 μmol/L (Corning, Corning, NY, USA). RAW 264.7 cells (1×10^5) were grown in the lower chamber while Hepa1-6 cells (5×10^4) were grown in the upper chamber for 48 h.

2.4. Cell viability assay

The cytotoxic effects of PEG-AuNPs against RAW264.7 and Hepa1-6 cells were evaluated using the CCK-8 assay. Briefly, RAW264.7 and Hepa1-6 cells were seeded in 96-well plates with a density of 1×10^4 per well and cultured for 12 h. Then, the cells were incubated with a series of different concentrations of PEG-AuNPs for 48 h followed by 10 μL CCK-8 reagent added, and the cells were incubated with the reagent for another 2 h. After that, the absorbance of each well was obtained at 450 nm and cell viability was calculated as shown in Eq. (1):

$$\text{Cell viability } (\%) = [(A_T - A_B)/(A_C - A_B)] \times 100 \tag{1}$$

where A = absorbance, T = treatment, B = blank, C = control.

2.5. Flow cytometry

The cells were detached from the cell culture plate, washed, and resuspended in phosphate-buffered saline (PBS). After then, the cells were trypsinized, and stained with FITC-conjugated F4/80 antibody and PE-conjugated CD206 or CD80 antibodies for 30 min at 4 °C. After then, the cells were washed with PBS extensively. Finally, the cells were suspended in PBS and flow cytometry (FACSVerse™, BD BioSciences, CA, USA) was performed to analyze the fluorescence of the cells.

2.6. ELISA

The concentrations of IL-10 and IL-12 in the cell media were assayed using an ELISA Kit (R&D Systems Inc.) according to the manufacturer's instructions. In brief, all reagents, samples, and standards were prepared as instructed. Then 50 μL standard or sample was added to the wells, and a 50 μL antibody cocktail was added. After incubation at 25 °C for 1 h, the liquid was removed and each well was washed with PBS three times. 3,3′,5,5′-Tetramethylbenzidine (TMB) solution was added to each well and incubated for 30 min. Then, stop solution was added and the absorbance was acquired at 450 nm. Finally, the expression of cytokines was normalized to the cell number in the ELISA-based analysis.

2.7. Real-time quantitative reverse transcription-polymerase chain reaction (RT-qPCR)

RNA was extracted with the RNA Fast 200 Extraction Kit according to the manufacturer's protocol. After that, RNA was converted to cDNA using PrimeScript™ RT Master Mix according to the manufacturer's protocol. qPCR analysis was carried out with SYBR Premix Ex Taq™ in a LightCycler quantitative PCR machine (Stratagene, Santa Clara, CA, USA). The levels of mRNA expression were normalized to that of glyceraldehyde 3-phosphate dehydrogenase (Gapdh).

2.8. Animal

All male BALB/c mice (18−20 g) raised under specific pathogen-free (SPF) conditions were bought from Shanghai SLAC Laboratory Animal Co., Ltd. (Shanghai, China). All experimental procedures were executed according to the protocols approved by the Committee on Animals of the Naval Medical University (Shanghai, China) and are in line with the internationally accepted standards.

2.9. In vivo antitumor assays of PEG-AuNPs

The in vivo antitumor assay of PEG-AuNPs was conducted in mice model bearing subcutaneous and xenografted liver cancer. Briefly, Hepa1-6 cells (4×10^6) were inoculated subcutaneously into the right flank of BALB/c mice with or without PEG-AuNPs (0.02 mg/kg or 0.1 mg/kg). After 7 days, the tumor volume was measured with the following formula (width^2 × length):/2. After 21 days, the mice were euthanized, and the tumor was excised and weighed to assess therapeutic efficacy. The inhibitory rate of tumors (IRT) was calculated as shown in Eq. (2):

$$\text{IRT } (\%) = [(W_e - W_c) / W_c] \times 100 \tag{2}$$

where W_e and W_c are the tumor weights of the experimental and control groups, respectively). On Days seven and 14, a subset of mice was euthanized, and their tumor tissues were harvested for immunofluorescence and TAM assays.

To investigate the effects of PEG-AuNPs upon the immune cells in the tumor environment, the dendritic cells (DCs) and T cells in the tumor tissues excised on Day 14 was analyzed as described below. Briefly, the tumor tissue was cut into pieces, and 1 mL of type IV collagenase (0.05 mg/mL) digested solution was added. The mixture was placed in a 37 °C water bath for continuous shaking for 1 h until the tumor tissue was dissociated into single cells. After then, the cell suspension was passed through a sterile 70 μm cell strainers and centrifuged at $1000 \times g$ for 5 min to remove the supernatant. The ACK (ammonium-chloride-potassium) lysis buffer was added to the cell debris to lyse erythrocytes by incubation at 25 °C for 3 min. Excessive PBS buffer was then added to terminate the lysis, and the supernatant was discarded by centrifugation at $1500 \times g$ for 5 min. The cell suspension was re-suspended by PBS and passed through a sterile 70 μm cell strainers. The cell density in the suspension was adjusted to be around 1×10^6/mL. DCs and T cells were stained with indicated antibodies to detect matured DCs (CD11$^+$CD86$^+$), CD3$^+$CD4$^+$ T cells and CD3$^+$CD8$^+$ T cells.

Formalin-fixed and paraffin-embedded tumors excised on Day 14 were also stained for Tunel (TdT-mediated dUTP nick end labeling) and KI67 using the procedure described below. Briefly, the excised tumors were fixed in PBS containing 4% para-formaldehyde and cut into 4 μm slices. The paraffin embedded slices were dewaxed to water, and the working solution of protease K was used for antigen repair. PBS containing 3% H_2O_2 was added to slices, and Tunel staining was performed using the Tunel Kit. KI67 staining was carried out using the KI67 antibody as the primary antibody and horseradish peroxidase (HRP)-conjugated goat anti-rabbit as the secondary antibody. Fresh diaminobenzidine (DAB) chromogenic solution was used for immunohistochemical staining, and hematoxylin was used to stain the nuclei. Finally, the slices were sealed by neutral gum and observed under microscope.

To elucidate the role of macrophages on the anticancer efficacy of PEG-AuNPs, we used clodronate liposomes to eliminate the macrophages of mice in vivo. Briefly, mice were given 200 μL of anionic clodronate liposomes (clophosome-A-clodronate liposomes, FormuMax) intraperitoneally once every 4 days for a total of three times. Four days after the last injection of clodronate liposomes, Hepa1-6 cells (4×10^6) were inoculated subcutaneously

into the right flank of BALB/c mice with or without the addition of PEG-AuNPs (0.02 mg/kg or 0.1 mg/kg). After 7 days, the tumor volume was measured, and after 21 days, the mice were euthanized, and the tumor was excised and weighed to assess therapeutic efficacy. On Day 14, a subset of mice was euthanized, and their tumor tissues were harvested for immunofluorescence and TAM assays.

2.10. Isolation of in vivo TAMs

The isolation of TAMs from solid tumors was carried out with the double Percoll density gradients-based method. Briefly, the solid tumors were enzymatically digested. After the solid tumors were dissociated into single cells, these cells were centrifuged to obtain a single-cell suspension. Then, the enrichment of tumor macrophages from the tumor cell suspension was carried out with double Percoll density gradients (35% and 45%), and the enriched cell suspensions were stained with PE-conjugated F4/80 antibody, followed by being stained with magnetic beads coupled with anti-PE antibody, and sorted with the LS MACS columns (Miltenyi Biotec, Bergisch Gladbach, Germany).

2.11. Western blotting

Western blotting was carried out according to a standard protocol as described below. In brief, cell extracts (30 μg protein) were loaded and separated by the sodium dodecyl sulfate-polyacrylamide gel electrophoresis (SDS-PAGE). After separation, the proteins were transferred to polyvinylidene difluoride (PVDF) membranes at 250 mA for 90 min. After being blocked with 5% skim milk, the PVDF membranes were incubated with anti-mouse LC3, beclin1, P62/sequestosome 1 (SQSTM1), or β-actin primary antibodies overnight at 4 °C, respectively. Then, the membrane was washed with PBS for 3 times and incubated with HRP-conjugated-goat anti-mouse IgG secondary antibody for another 2 h. The results were acquired by Odyssey system (LI-COR, Lincoln, NE, USA).

2.12. The transfection of mRFP-GFP-LC3 adenovirus

RAW 264.7 cells (1×10^5) were inoculated in the lower Transwell® chamber and transfected with mRFP-GFP-LC3 adenovirus for 6 h at a multiplicity of infection (MOI) of 100. The transfected macrophages were incubated with DMEM containing 10% FBS for another 48 h before TSN co-culturing. Autophagosomes (green$^+$red$^+$) and autolysosomes (Green$^-$Red$^+$) were observed and calculated by confocal microscopy (Leica TCS SP8, Leica, Biberach, Germany). To analyze the autophagy flux, the ratio of fluorescent punctae/cell was calculated by dividing the punctae number by the cell number.

2.13. Lysosomal acidity and stability assay

Lysosomal acidity and stability assays were performed as described previously[35]. TSN co-cultured RAW 264.7 cells were treated with PEG-AuNPs (10 or 50 μmol/L) for 48 h. For the lysosomal acidity assay, the cells were washed twice with PBS then stained with 100 nmol/L LysoSensor Green DND-189 dye dissolved in pre-warmed medium for 30 min at 37 °C. After staining, the cells were observed with a fluorescence microscope (Olympus IX71, Tokyo, Japan). The cells were then collected and analyzed by flow cytometry. Lysosomal stability assay was performed as described below. In brief, the cells were washed twice and then treated with 20 μg/mL acridine orange (AO) dissolved in pre-warmed medium for 15 min at 37 °C. After AO staining, the cells were washed, collected, and analyzed for their red fluorescence by flow cytometry.

2.14. Atg5 siRNA transfection

Small interfering RNA (siRNAs) against Atg5 and a non-specific scrambled siRNA were synthesized by Gene pharm Biotech, and transfected using Lipofectamine 2000 according to a standard protocol. Briefly, after cells were grown to 80% confluence, the cells were transfected with 20 pmol siRNA with Lipofectamine 2000 for 6 h. After then, a fresh medium was added to the cells. Twenty-four hours later, RT-qPCR was carried out to evaluate the gene expression.

2.15. Investigation of the endocytosis mechanism of nanoparticles in macrophages

The uptake mechanism of PEG-AuNPs was investigated in TSN co-cultured RAW 264.7 cells. Briefly, RAW 264.7 cells were cultured on 6-well plates at a density of 1.5×10^5 cells per well overnight. RAW 264.7 cells were treated with one of the following inhibitors for 1 h before the treatment of PEG-AuNPs: dynasore (100 μmol/L); chlorpromazine (100 μmol/L). Then, the cells were washed with PBS to remove all the inhibitors and incubated with the medium containing 50 μmol/L PEG-AuNPs for 1 h. After that, the cells were washed three times, tryptic digested, and collected for ICP-AES assay.

2.16. Statistical data analysis

Statistical data analysis was carried out using GraphPad Prism 5.0 (GraphPad Software, Inc., San Diego, CA, USA). The results are presented as means ± standard deviation (SD). Statistical analysis was performed using Student's unpaired t-test or analysis of variance (ANOVA). $^*P < 0.05$; $^{**}P < 0.01$; $^{***}P < 0.001$.

3. Results and discussion

3.1. Characterization of PEG-AuNPs

The AuNPs have been investigated widely recently due to their superior biocompatibility, tunable size, and optical properties[36]. PEGylation of AuNPs could greatly improve their solubility and stability in aqueous solutions[37]. Therefore, we successfully synthesized PEG-AuNPs with a series of sizes (5, 20, 50, and 100 nm) using the sodium borohydride reduction method (Fig. 1A). The size, uniform distribution, and spherical shape of the PEG-AuNPs were evaluated by TEM (Fig. 1B). As the particle size increased, the color of the PEG-AuNPs gradually lightened (Fig. 1C), while the wavelength of maximum absorbance gradually red-shifted (Fig. 1D). These results verified the synthesized gold nanoparticles met desired size, shape, and structure. The size of PEG-AuNPs did not change significantly at the storage period of 14 days, suggesting their good stability (Supporting Information Fig. S1).

We then performed cell viability assays to evaluate the cytotoxicity of PEG-AuNPs against RAW 264.7 and Hepa1-6 cells. As shown in Supporting Information Fig. S2, the results showed that
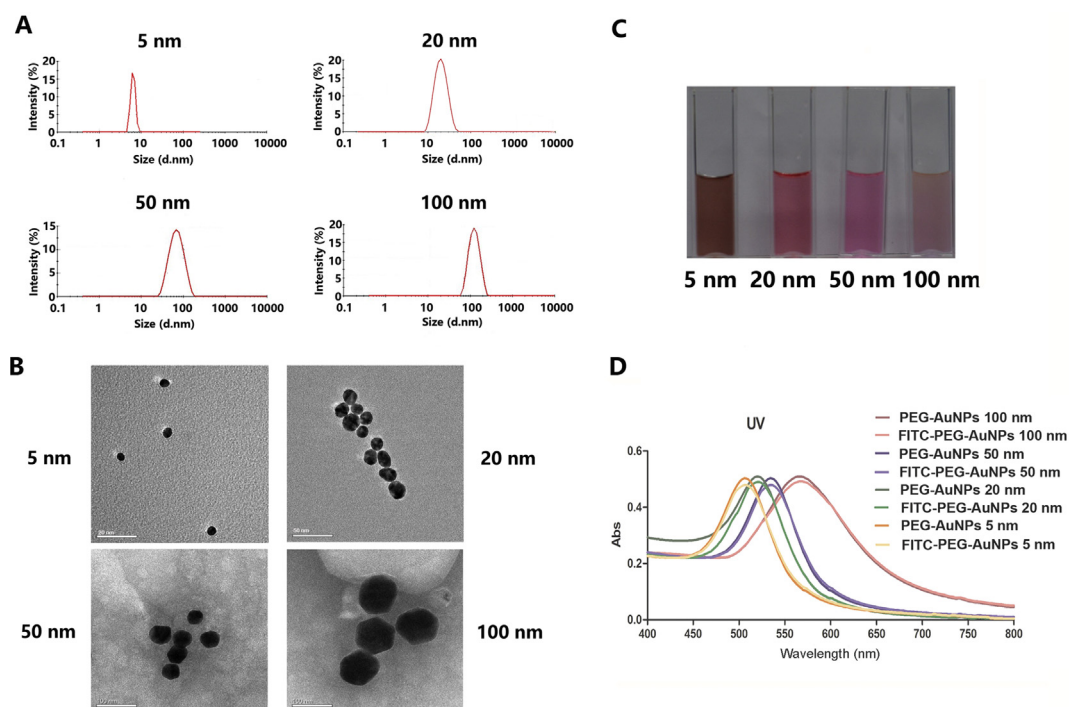
Figure 1 Characterization of PEG-AuNPs. (A) The size of PEG-AuNPs was measured with dynamic light scattering (DLS). (B) TEM images of PEG-AuNPs. Scale bar = 20, 50 or 100 nm. (C) Photographs of PEG-AuNPs in aqueous suspension. (D) UV−Vis absorption spectra of PEG-AuNPs or FITC-labeled AuNPs at wavelengths from 400 to 800 nm.

the cytotoxicity of PEG-AuNPs was in concentration dependent manner where the cytotoxicity increased when the cells incubated with high concentration PEG-AuNPs. The PEG-AuNPs with a particle size of 20 nm owned the optimal biocompatibility. At concentrations less than 50 μmol/L, there was no significant cytotoxic effect of 20 nm PEG-AuNPs towards RAW 264.7 and Hepa1-6 cells.

3.2. The cellular uptake of PEG-AuNPs in TAMs

TAMs are good targets for nanomaterials, mainly because materials at the nanosize level have natural targeting on macrophages, and thus macrophages have a strong phagocytic effect on them[38]. To investigate the relationship between the size of PEG-AuNP and cellular uptake efficiency, we treated RAW 264.7 and Hepa1-6 cells with 5, 20, 50, and 100 nm PEG-AuNPs for 4 h. The concentration of PEG-AuNPs in the cell suspensions was quantitatively measured using inductively coupled plasma-atomic emission spectroscopy (ICP-AES)[39]. As shown in Fig. 2A, the results showed that the cellular uptake of PEG-AuNPs was size-dependent, and nanoparticles of five and 20 nm were most readily internalized by macrophages and cancer cells. It has been reported[39,40] that the cellular uptake of nanoparticles was closely associated with the size, and nanoparticles of smaller size would have better cellular penetration. Especially, the diameter of AuNPs smaller than 10 nm has been reported to show superior localization and penetration in cancer cells than those larger than 10 nm[39]. Our results also demonstrated that nanoparticles with smaller sizes could have increased cellular uptake compared with larger nanoparticles.

It has been reported[41] that the tumor microenvironment can induce macrophages to polarize toward the M2 phenotype, which is due to the soluble factors derived from tumor cells. Evidence has shown that TSN can induce RAW264.7 cells to polarize towards M2 TAMs[41,42]. Herein, we co-incubated the RAW2 64.7 cells with Hepa1-6-cells using Transwell® plates and assessed the expression of M2 surface marker CD206. After co-culture with cancer cells for 48 h, the percentage of CD206⁺F4/80⁺ macrophages were considerably higher in the TSN group (75.4%) compared with the control group (27.2%) ($P < 0.001$), indicating macrophage polarization toward the M2 phenotype after co-culture with TSN (Fig. 2B). IL-10 is a characteristic cytokine highly expressed in M2 macrophages[16]. Thereby, we detected the secretion of IL-10 using ELISA in the macrophages co-culturing with TSN for 12, 24, 36 and 48 h. The IL-10 level increased with the extension of time in the TSN group ($P < 0.01$), whereas no substantial change was observed in the control group, further demonstrating the polarization of macrophages toward the M2 phenotype in the presence of TSN in a time-dependent manner (Fig. 2C). We then conducted an RT-qPCR assay to detect the M2 phenotype-related markers (*Arg1* and *Cd163*) and found them to be upregulated in the TSN co-culture group in comparison to the control group ($P < 0.001$) (Fig. 2D). These data suggest that macrophage polarization was successfully induced by co-culturing with TSN *in vitro*.

Next, we evaluated the cellular uptake of PEG-AuNPs in TSN co-cultured RAW264.7 cells. The five and 20 nm PEG-AuNPs showed the greatest uptake by macrophages (Fig. 2E). In addition, we further used TEM to detect the intracellular location of the differently sized PEG-AuNPs in TAMs. The TEM images confirmed that five and 20 nm PEG-AuNPs are located in the cytoplasm and distributed in large numbers around the nucleus and these nanoparticles were found to be evenly distributed in the cells (Fig. 2F). However, few PEG-AuNPs with diameter of 50 and
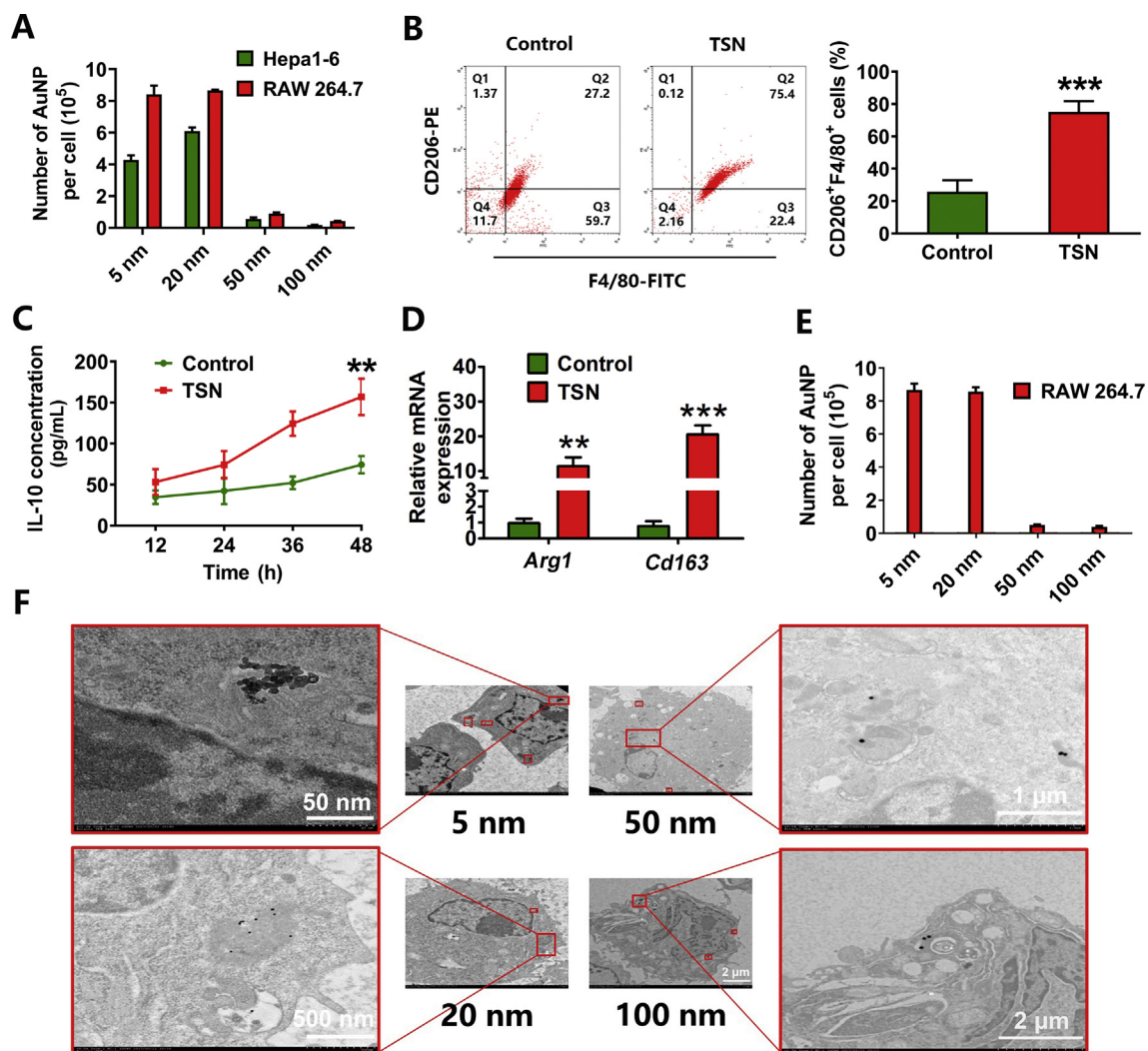
Figure 2 The cellular uptake and penetration of PEG-AuNPs. (A) Quantitative ICP-AES measurement of PEG-AuNPs uptake in RAW264.7 and Hepa1-6 cells. (B) The analysis of the $CD206^+/F4/80^+$ cells was performed with flow cytometry in RAW264.7 cells cocultured with TSN for 48 h; (C) The IL-10 concentration of supernatant from RAW 264.7 cells co-cultured with TSN at different time points as measured using ELISA; (D) The levels of the M2 phenotype related genes *Arg1* and *Cd163* mRNA were measured using RT-qPCR in RAW264.7 cells co-cultured with TSN for 48 h; (E) Quantitative ICP-AES measurement of PEG-AuNPs uptake in RAW264.7 cells co-cultured with TSN; (F) TEM images of PEG-AuNPs uptake and penetration in TAMs. Data are expressed as mean ± SD ($n = 5$). **$P < 0.01$, ***$P < 0.001$. Scale bar = 50 nm, 500 nm, 1 μm and 2 μm.

100 nm were presented in cells, whose cellular penetration was not as efficient as that of the small-sized nanoparticles. These results demonstrated that the cellular uptake and penetration of PEG-AuNPs in TAMs were size-dependent, and smaller nanoparticles (diameter of five and 20 nm) possess improved cellular uptake penetration. Our results were consistent with the studies investigating the cellular uptake of nanoparticles of different sizes[43].

Subsequently, we investigated the endocytosis mechanisms of nanomaterials. There are four types of endocytosis mechanisms of nanomaterials: phagocytosis, macropinocytosis, clathrin, and caveolin-mediated endocytosis pathways[44]. Phagocytosis and macropinocytosis are actin-dependent endocytic pathways that mediate the uptake of nanomaterials[45], whereas clathrin or caveolin-mediated endocytosis is the manner by which substance enters into the cells through the plasma membrane by clathrin or caveolin-coated vesicles which are formed by the contraction

effect of dynamin[46]. Dynasore is a specific inhibitor of endocytic pathways that prevents the formation of dynamin[47]. As shown in Supporting Information Fig. S3, dynasore treatment substantially inhibited the internalization of PEG-AuNPs of 5, 20 and 50 nm, suggesting that the endocytosis of PEG-AuNPs of 5, 20, and 50 nm may in principle adopt clathrin or caveolin mediated endocytosis. On the contrary, an obvious inhibition effect was not observed for PEG-AuNPs of 100 nm. Furthermore, the endocytosis of PEG-AuNPs of 5, 20, and 50 nm was also significantly suppressed by chlorpromazine which could inhibit the formation of clathrin-coated vesicles, whereas the uptake of PEG-AuNPs of 100 nm was not influenced by these inhibitors, suggesting that endocytosis pathway of PEG-AuNPs of 100 nm was not clathrin and caveolin mediated. In the case of the large size of PEG-AuNPs of 100 nm, their endocytosis may mainly go through the macropinocytosis pathway[44].

Since the 20 nm PEG-AuNPs showed the lowest toxicity and most effective cellular uptake in TAMs, we used 20 nm PEG-AuNPs in the subsequent experiments.

3.3. PEG-AuNPs suppress M2 macrophage polarization in vitro

To investigate the effects of PEG-AuNPs on macrophage polarization in vitro, we incubated TSN cultured macrophages with PEG-AuNPs of 20 nm for 48 h, and the macrophage cell surface proteins CD80 and CD206 were evaluated by flow cytometry[16]. PEG-AuNPs did not change the CD80 expression of TSN co-cultured macrophages, but significantly decreased the CD206 expression (Fig. 3A and B). Then, the secretion of cytokines IL-12 (M1 phenotype) and IL-10 (M2 phenotype) was assessed using ELISA. The results demonstrated that the production of IL-10 was substantially decreased by PEG-AuNPs, whereas PEG-AuNPs did not affect the secretion of IL-12 (Fig. 3C). Furthermore, PEG-AuNPs could significantly reduce the mRNA levels of *Arg1* and *Cd163* (M2 genes) but did not affect the expression of *Tnf-α* and inducible nitric oxide synthase (*Inos*) (M1 gene) (Fig. 3D). Pal et al.[17] have demonstrated that AuNPs could downregulate IL-10 but also upregulate IL-12 in TAMs, resulting in the polarization of the M2 to M1 phenotype for TAMs. Consistently, our results indicated that PEG-AuNPs could inhibit the M2 polarization of TAMs, as reflected by reduced expression of M2 markers such as CD206, *Cd163*, *Arg1*, and IL10.

3.4. In vivo inhibition of subcutaneous tumor growth and M2 macrophage polarization by PEG-AuNPs

To determine whether PEG-AuNPs could affect tumor growth in vivo, Hepa1-6 cells were injected subcutaneously into the right flank of male BALB/c mice, with or without the addition of 20 nm PEG-AuNPs. As shown in Fig. 4A, the results showed that the tumor volume was substantially decreased with PEG-AuNPs injection, and a higher dose of PEG-AuNP (50 μmol/L) showed better therapeutic efficacy compared with the lower dose (10 μmol/L) (Fig. 4A). Consistently, the average final tumor weight of mice treated with the higher dose of PEG-AuNP was lower in comparison to that of mice treated with the lower dose of

PEG-AuNPs ($P < 0.05$) (Fig. 4B and C). To evaluate whether PEG-AuNPs could reprogram TAM polarization in vivo, the PEG-AuNPs treated tumors and TAMs were analyzed using immuno-fluorescence staining, flow cytometry and RT-qPCR. In tumor slices obtained on Days seven and 14 after implantation, the number of CD206$^+$ cells were lower in the PEG-AuNPs-co-injected tumors than in the control tumors, suggesting that the number of M2 TAMs was reduced by PEG-AuNPs treatment (Fig. 4D). The tumor tissues obtained on Days seven and 14 were enzymatically digested to isolate TAMs, and the expression of F4/80 and CD206 (M2 TAM markers) was quantified using flow cytometry. The number of CD206$^+$/F4/80$^+$ cells in the PEG-AuNPs co-injected tumors was significantly decreased in comparison to that of controls (Fig. 4E). On Days seven and 14, the mRNA levels of *Arg1*, *Cd163*, and *Il-10* (M2 markers) in the TAMs of PEG-AuNPs co-injected tumors were significantly reduced compared with those in controls (Fig. 4F). To elucidate whether PEG-AuNPs have direct activity to tumor cells and the role of macrophages on the anticancer efficacy of PEG-AuNPs, we used clodronate liposomes to eliminate the macrophages of the mice in vivo. Then, Hepa1-6 cells were inoculated subcutaneously into the BALB/c mice with or without PEG-AuNPs. After 14 days, the mice were euthanized, and the tumor was excised and weighed to assess therapeutic efficacy. The results showed that PEG-AuNPs treatment did not show any therapeutic efficacy, as reflected by the fact that the average final tumor weight of mice did not differ among all the three groups (Supporting Information Fig. S4A–C). In tumor sections obtained on Day 14 after implantation, F4/80$^+$ and CD206$^+$ cells disappeared in all the groups (Fig. S4D). These results suggested that PEG-AuNPs have no direct therapeutic efficacy towards tumors, and the elimination of macrophages abrogated the therapeutic efficacy of PEG-AuNPs.

Subsequently, the immune profiles in tumor microenvironment was analyzed after treatment with PEG-AuNPs. Fig. 5A and B showed that PEG-AuNPs effectively elicited the maturation of dendritic cells (DCs). 0.02 mg/kg and 0.1 mg/kg PEG-AuNPs significantly promoted the maturation of DCs, which was 2- and 4-fold than that of control group, respectively. As shown in Fig. 5C−F, PEG-AuNPs effectively increased the frequency of CD3$^+$CD4$^+$ T cells and CD3$^+$CD8$^+$ T cells in tumors, while
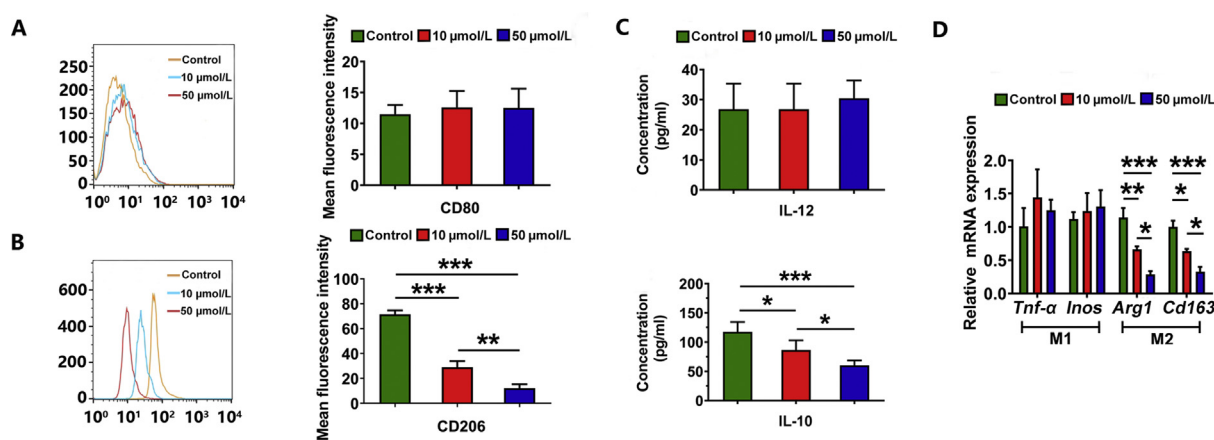

Figure 3 PEG-AuNPs suppress the polarization of macrophages to the M2 phenotype *in vitro*. TSN co-cultured RAW264.7 cells were treated with or without PEG-AuNPs for 48 h at concentrations of 10 and 50 μmol/L, respectively. The expression of (A) CD80 and (B) CD206 of macrophages was evaluated using flow cytometry. (C) The concentrations of IL-12 and IL-10 of macrophages were analyzed using ELISA. (D) The mRNA levels of *Tnf-α*, *Inos*, *Arg1* and *Cd163* of macrophages were measured using RT-qPCR. Data are expressed as mean ± SD ($n = 5$). *$P < 0.05$, **$P < 0.01$, ***$P < 0.001$.
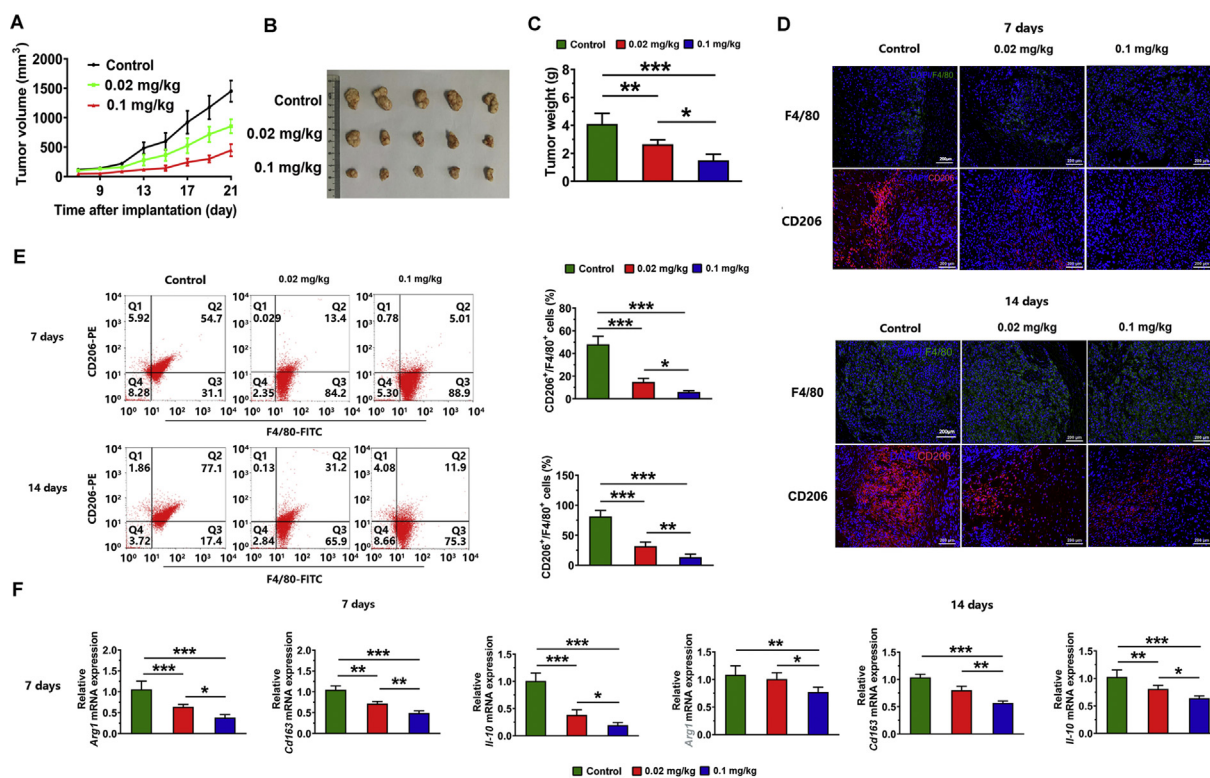
Figure 4 *In vivo* antitumor activity and inhibition of M2 macrophage polarization by PEG-AuNPs. (A) Tumor growth curves. Hepa1-6 cells were subcutaneously inoculated into the right flank of male BALB/c mice with or without 20 nm PEG-AuNPs, and the tumor growth was monitored for 21 days. (B) The gross images of excised tumors from the mice at the endpoint. (C) Tumor weight at the endpoint. (D) Representative immunofluorescence staining of $CD206^+$ and $F4/80^+$ macrophages in tumor tissues on Days seven and 14 after implantation. Scale bar = 200 μm. (E) $CD206^+/F4/80^+$ macrophages were analyzed using flow cytometry in tumor tissues on Days seven and 14 after implantation. (F) The mRNA levels of genes (M2 phenotype) measured using RT-qPCR in tumors on Days seven and 14 after implantation in mice. Data are expressed as mean ± SD (*n* = 5). *$P < 0.05$, **$P < 0.01$, ***$P < 0.001$.

0.1 mg/kg PEG-AuNP exhibited the highest proportion of T cells among all treatment groups. Cell proliferation and apoptosis in the tumor environment are also detected by KI67 and Tunel staining, respectively. As shown in Fig. 5G–J, after treatment with PEG-AuNPs, immunohistochemical staining revealed a significant decrease in KI67 expression and increase in Tunel staining, suggesting that the reduced tumor cell proliferation and increased tumor cell apoptosis.

Taken together, these data indicate that PEG-AuNPs can inhibit the polarization of TAMs to the M2 phenotype *in vivo*, thereby reducing the immunosuppressive effects and initiating antitumor immunotherapy. M1 macrophages possess intrinsic function to phagocytose tumor cells, and could also secret immuno-stimulatory cytokines (IL-6, IL-12, TNF et al.) to activate other immune cells including dendritic cells and T cells[48]. We have demonstrated that, after elimination of macrophages, the therapeutic efficacy of PEG-AuNPs was abrogated, suggesting the pivotal role of macrophages in the antitumor activity of PEG-AuNPs, and that PEG-AuNPs have no direct therapeutic efficacy towards tumor cells. After treatment with PEG-AuNPs, the proportion of mature dendritic cells, $CD3^+CD4^+$ T cells and $CD3^+CD8^+$ T cells increased significantly, accompanied with significantly increased proportion of apoptotic tumor cells. The results suggested that PEG-AuNPs could inhibit the polarization of TAMs to the M2 phenotype and activate other immune cells including dendritic cells and T cells, thus eliciting antitumor immunity and consequent tumor suppression. Similarly, several kinds of nanomaterials have been reported to regulate the polarization of TAMs and play an active role in regulating biological effects[14,38,49]. For example, iron oxide nanoparticles can induce the polarization of macrophages to the M1 phenotype, increase the level of reactive oxygen species (ROS) and TNF-α, and inhibit mammary tumor growth and liver and lung metastasis[14]. The cationic polymers, cationic dextran, and polyethyleneimine (PEI), can also reverse the polarization of TAMs through toll-like receptor 4 (TLR-4) to promote IL-12 expression, thereby facilitating cancer immunotherapy[50]. Also, several nanomaterials, such as silver and zinc oxide nanoparticles, can modulate macrophage polarization[38]. Therefore, the use of nanomaterials to reverse M2 TAMs for cancer immunotherapy is a promising treatment strategy.

3.5. PEG-AuNPs block autophagic flux in TAMs

Autophagy is a dynamic cellular process, which is characterized by the formation of autophagosomes, fusion of lysosomes and autophagosomes, formation of autophagolysosomes, and subsequent degradation[51]. Autophagy is strictly regulated by a variety of proteins, including autophagy-related proteins (ATG), LC3, P62/SQSTM1, and beclin1[52]. LC3 is a kind of autophagosome marker, and LC3 has two forms: LC3-I, which is a 16 kDa cytosolic protein, and LC3-II, which is a processed 14 kDa form.
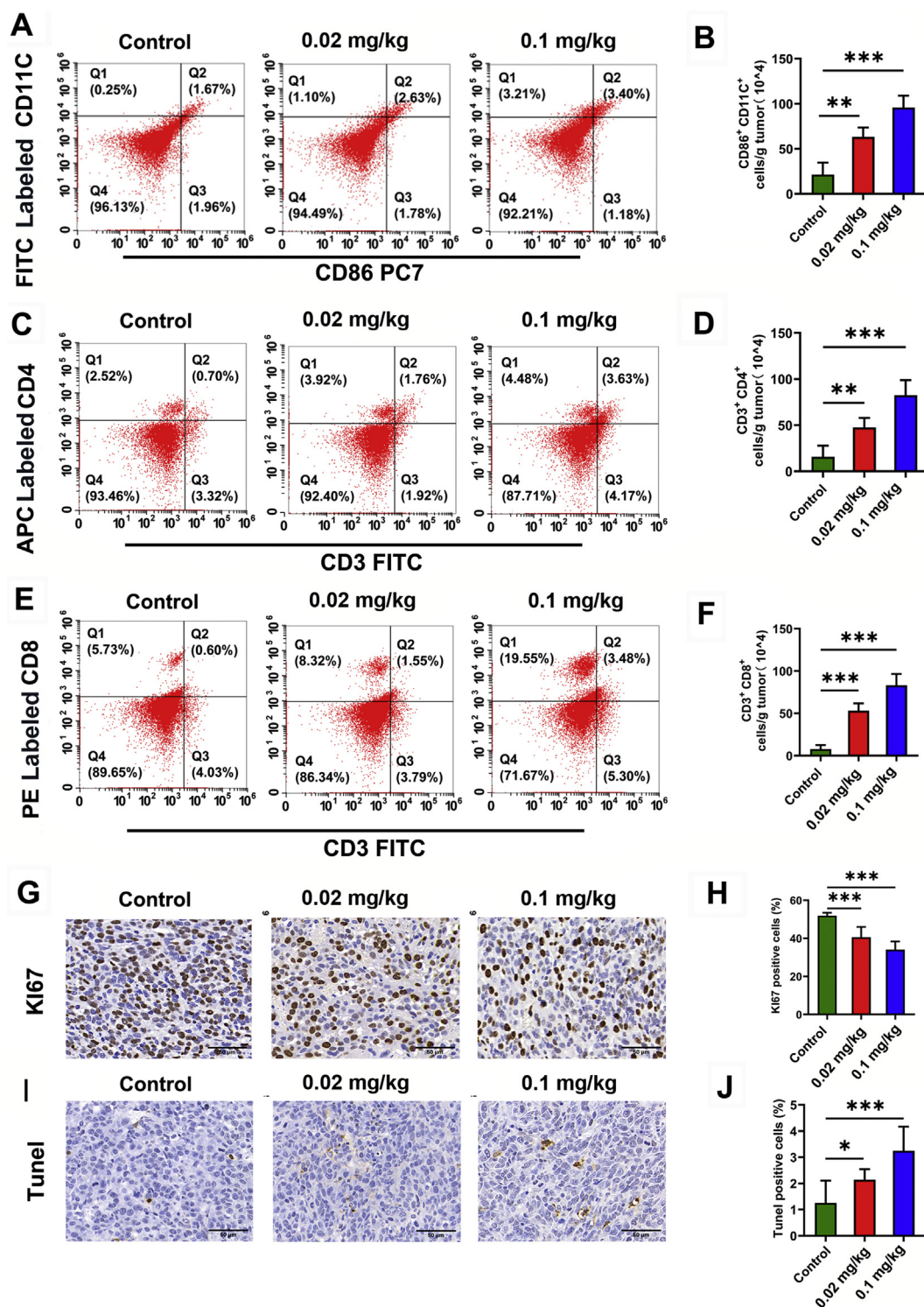
Figure 5 The effects of PEG-AuNPs on the immune cells and tumor cells in the tumor environment. (A) Representative flow cytometry plots and (B) quantitative analysis of mature DCs (CD11$^+$CD86$^+$) in tumors. (C) Representative flow cytometry plots and (D) quantitative analysis of CD3$^+$CD4$^+$ T cells in tumors. (E) Representative flow cytometry plots and (F) quantitative analysis of CD3$^+$CD8$^+$T cells in tumors. Data are expressed as mean $\pm$ SD ($n = 6$). (G) Representative images and (H) quantitative analysis of KI67 staining in tumors. (I) Representative image and (J) quantitative analysis of Tunel staining in tumors. Scale bar $= 50$ μm. Data are expressed as mean $\pm$ SD ($n = 10$). *$P < 0.05$, **$P < 0.01$, ***$P < 0.001$.

The total amount of LC3 protein or the LC3-II/LC3-I ratio can reflect the level of autophagy[52]. P62/SQSTM1 (P62), a versatile adaptor protein, is a selective autophagy receptor[53]. Beclin1 is necessary for autophagosome formation by mediating autophagy protein localization in the phagophore, and its protein level is positively correlated with autophagy[54]. As shown in Fig. 6A, after TSN co-culture, the total amount of beclin1 and LC3 in macrophages increased substantially, with a decreased level of P62, indicating autophagy is activated in the TSN-cultured macrophages. After treatment with PEG-AuNPs, the total amount of LC3 protein continued to increase, with increased expression of P62 and decreased expression of beclin1, suggesting that PEG-AuNPs could block the autophagic flux of macrophages.

mRFP-GFP-LC3 (mRFP is a red fluorescent marker, and GFP is a green fluorescent marker) was used to further monitor autophagic flux[55]. In the initial stage of autophagy, mRFP-GFP-LC3 aggregates on autophagosomes, and red/green co-localized dots can be observed. At the later stage of autophagy, autophagosomes

are fused with lysosomes, resulting in the formation of autophagolysosomes. Since GFP is unstable and quenched under acidic conditions, only red fluorescent punctate can be detected at this stage. Therefore, autophagosomes in cells are labeled as yellow dots (the overlap of green and red fluorescence), and autophagolysosomes are labeled as red dots (the quenching of green fluorescence). Firstly, we transfected RAW264.7 cells with an mRFP-GFP-LC3 adenovirus, following which the macrophages were cultured with or without TSN and treated with PEG-AuNPs (10 or 50 μmol/L) for 48 h. Then, the mRFP-positive (R+) and GFP-positive (G+) dots were detected using confocal microscopy (Fig. 6B). The results showed that the numbers of yellow (G+R+) and red (G−R+) dots were substantially augmented after TSN co-culture, suggesting that autophagic flux was activated in TSN cultured macrophages. After incubation with PEG-AuNPs, the number of yellow dots (G+R+) in TSN-cultured macrophages was significantly increased, whereas the number of red dots (G−R+) was significantly decreased, suggesting that PEG-AuNPs inhibit
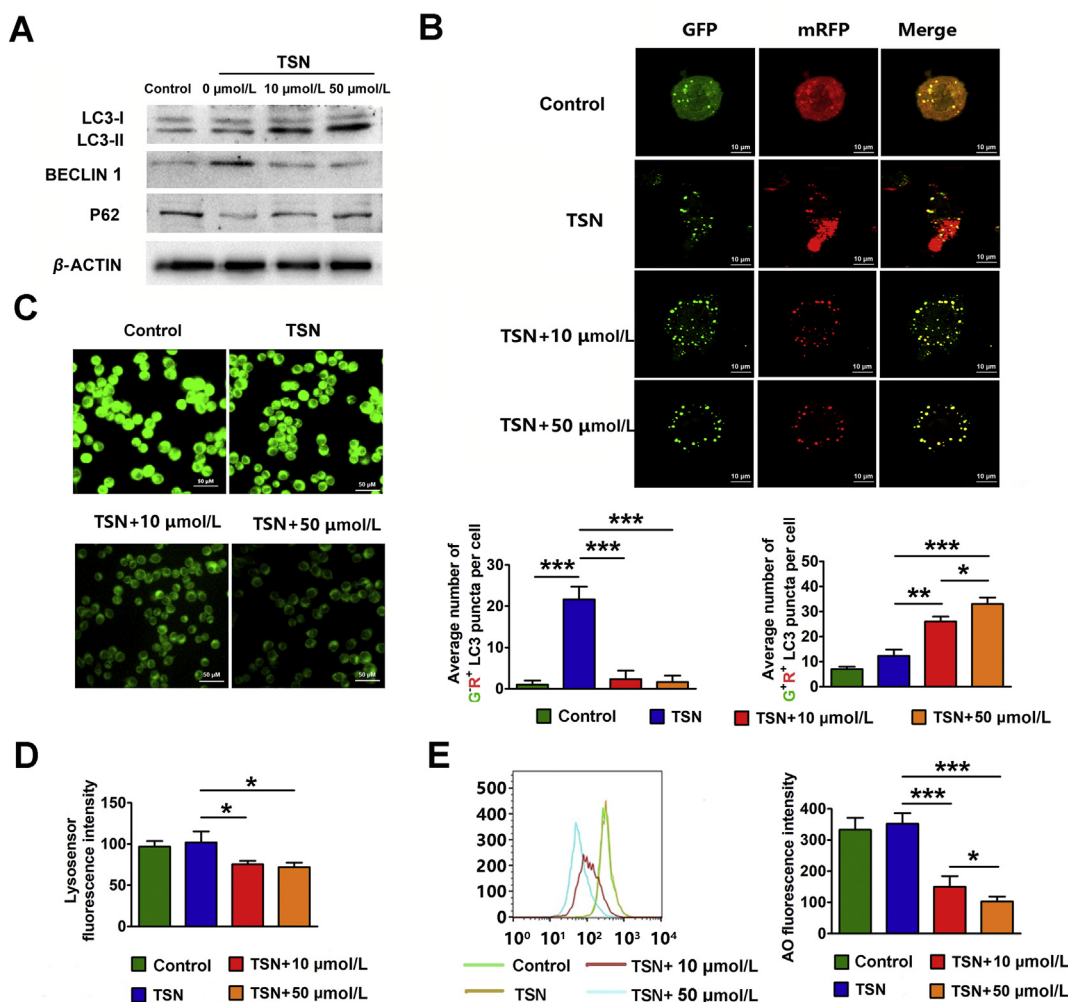

Figure 6 PEG-AuNPs block autophagic flux and cause lysosomal dysfunction in macrophages. (A) Western blotting analysis of autophagy-related proteins. (B) The images of representative immunofluorescence and quantitative analysis of the number of yellow autophagosomes (G+R+) and red autolysosomes (G−R+) of mRFP-GFP-LC3 dots in macrophages. Scale bar = 10 μmol/L. (C) Fluorescence images of LysoSensor Green DND-189 stained macrophages. Scale bar = 50 μmol/L. (D) Flow cytometry analysis of LysoSensor Green DND-189 stained macrophages. (E) Flow cytometry analysis of macrophages stained with acridine orange (AO). Data are expressed as mean ± SD ($n = 5$). $*P < 0.05$, $**P < 0.01$, $***P < 0.001$.
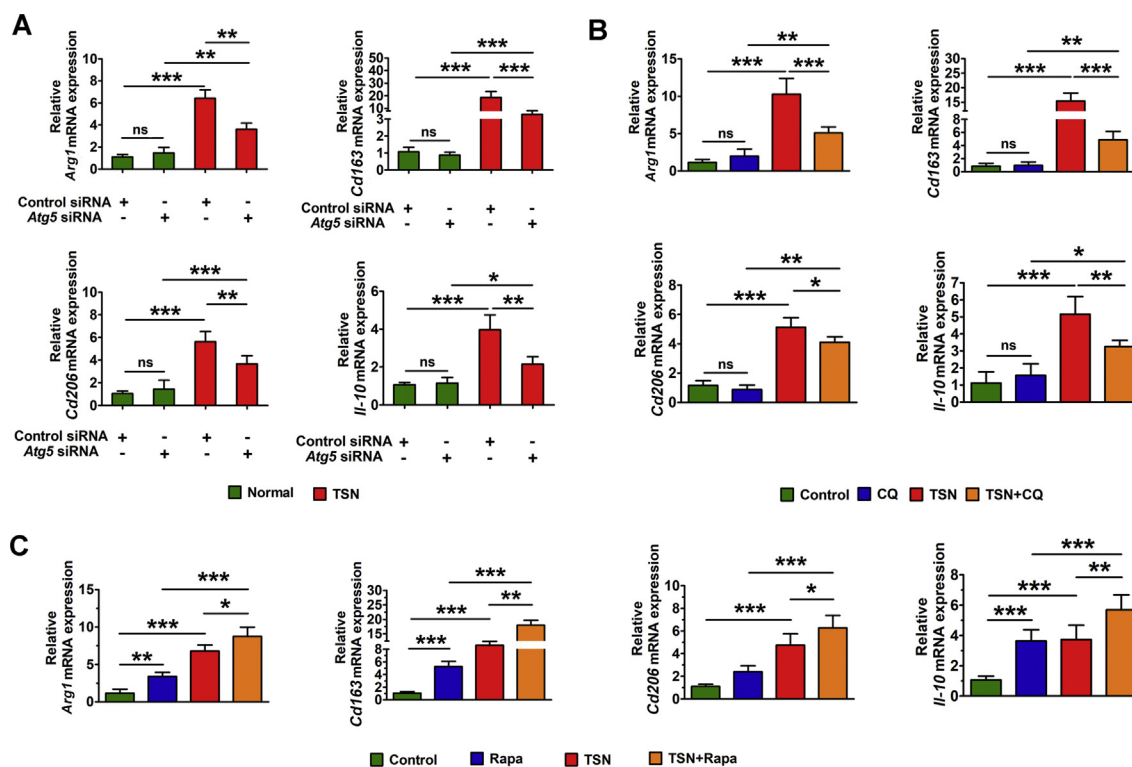
Figure 7 Inhibition of M2 macrophage polarization by autophagy blockade. Analysis of relative mRNA expression of *Arg1*, *Cd163*, *Cd206*, and *Il-10* in TSN co-cultured RAW 264.7 cells incubated with *Atg5* siRNA (A), chloroquine (CQ) (B), and rapamycin (Rapa) (C). Data are expressed as mean ± SD (n = 5). *P < 0.05, **P < 0.01, ***P < 0.001. ns, not statistically significant.

the formation of autophagolysosomes and induce the accumulation of autophagosome. Therefore, autophagic flux is blocked by PEG-AuNPs in TSN co-cultured macrophages.

To further clarify the mechanism underlying PEG-AuNPs-induced autophagic flux blockage, we explored the impact of PEG-AuNPs on the function of lysosomes in TAMs. The lysosome is an acidic compartment with a stable membrane structure, whereas lysosomal dysfunction will be induced with lysosomal alkalization and lysosomal membrane permeabilization[25,51]. As shown in Fig. 6C and D, by staining with LysoSensor Green DND-189, which is an indicator for detecting pH with fluorescence intensity, lysosomal acidification evaluated according to fluorescence intensity was markedly decreased in PEG-AuNPs treated TSN-cultured macrophages in comparison to that in control cells. Acridine orange (AO) is a lysosomotropic, metachromatic fluorescent dye that yields red fluorescence when they accumulate within the lysosomes[25]. Fig. 6E shows that PEG-AuNPs could decrease the red fluorescence intensity of AO in a concentration-dependent manner, suggesting the leakage of AO from the lysosome[32].

Altogether, our results firmly confirmed that PEG-AuNPs can cause lysosomal dysfunction by inducing lysosomal alkalization and lysosomal membrane permeabilization and therefore inhibit autophagic flux in TAMs. Accordingly, various nanomaterials have been demonstrated to induce lysosomal dysfunction, and one general type of lysosomal dysfunction related to nanomaterials treatment is lysosome membrane permeabilization, since nanomaterials are commonly sequestered within the lysosomal compartment[51].

3.6. Suppression of macrophages polarization to M2 phenotype by autophagy blockade

PEG-AuNPs suppressed M2 macrophage polarization and block autophagic flux. We subsequently investigated whether TAMs M2 polarization could be inhibited by autophagy blockade. The effects of a series of concentrations of autophagy inhibitors (chloroquine and *Atg5* siRNA) and autophagy inducers rapamycin were investigated on the polarization of TSN co-cultured macrophages. As shown in Fig. 7A, the mRNA expressions of *Arg1*, *Cd163*, *Cd206*, and *Il-10* were substantially increased in TSN co-cultured macrophages in comparison to that in normal cultured macrophages, suggesting that TSN co-culture promoted the M2 polarization. In normal cultured macrophages, after transfection with *Atg5* siRNA, no substantial difference in the expression of *Arg1*, *Cd163*, *Cd206*, and *Il-10* between the two groups was observed, indicating that autophagy inhibition itself could not induce M2 polarization. However, in TSN co-cultured macrophages, in comparison to the control siRNA group, the expression of *Arg1*, *Cd163* *Cd206*, and *Il-10* significantly decreased after *Atg5* siRNA transfection, indicating that autophagy inhibition could reduce the M2 polarization caused by TSN. Similarly, the Mrna expression of *Arg1*, *Il-10*, *Cd163*, and *Cd206* was substantially reduced in TSN co-cultured macrophages after treatment with 20 μmol/L chloroquine for 48 h (Fig. 7B). Meanwhile, following treatment with 100 nmol/L rapamycin for 48 h, the expression of *Arg1*, *Cd163*, *Cd206*, and *Il-10* in TSN co-cultured macrophages increased significantly, indicating that induction of autophagy can promote the M2 polarization (Fig. 7C). Therefore, these results
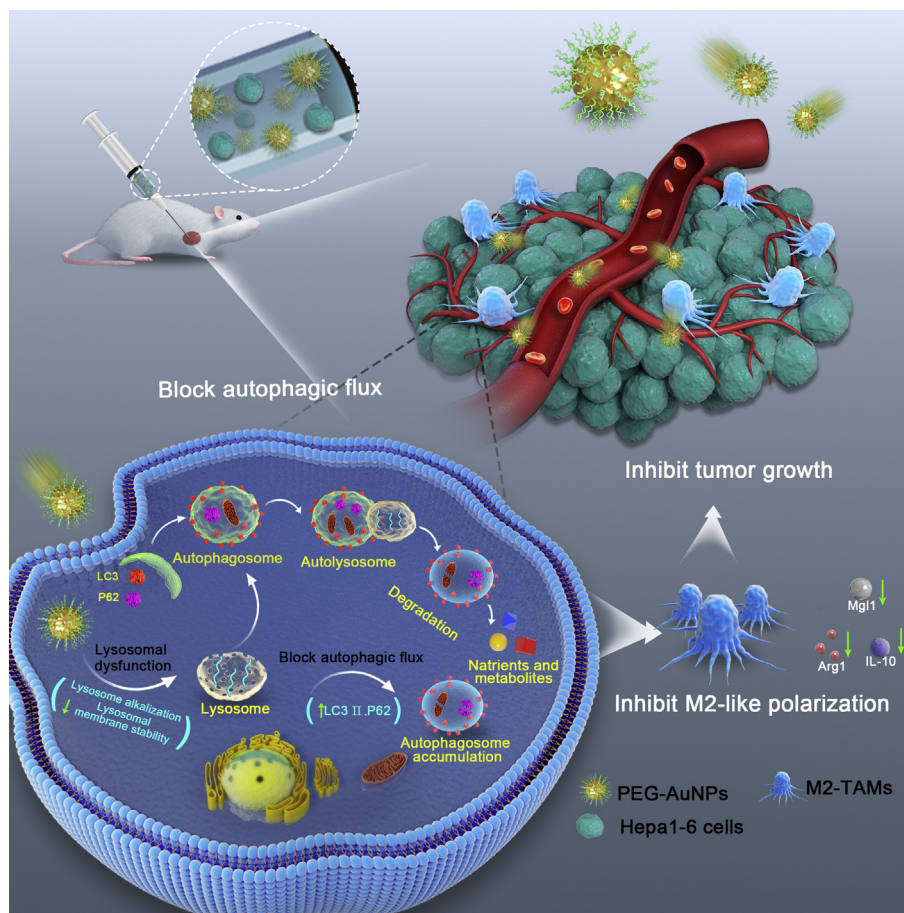
Figure 8 The schematic diagram of the mechanism underlying PEG-AuNPs-induced antitumor immunotherapy, involving inhibiting TAMs M2 polarization *via* induction of lysosome dysfunction and autophagic flux inhibition. After PEG-AuNPs internalization, the autophagic flux of TAMs was blocked due to lysosomal dysfunction, as reflected by autophagosome accumulation. After then, the M2 polarization of TAMs was inhibited, resulting in potential antitumor immunotherapy.

demonstrated that TSN culture could activate autophagy and polarize macrophages to the M2 phenotype, and autophagy blockade could suppress M2 macrophage polarization.

In this study, our results revealed the mechanism that PEG-AuNPs reduce TAMs M2 polarization *via* autophagy blockade. Autophagy has been shown to have an anti-inflammatory effect through downregulation of the inflammasome, an intracellular structure that promotes the generation of active proinflammatory cytokines[56,57], and recent reports of the nonspecific lysosomal inhibitors chloroquine and bafilomycin A1 impairing M2 polarization in the tumor microenvironment[58]. Furthermore, inhibition of autophagy will rescue NF-κB activity and force M2-polarized macrophages to produce a high level of M1-like cytokines[55]. Several small molecule drugs including neferine and baicin were shown to induce autophagy and reduce M2 polarization of macrophages[22,23]. The discrepancy between small molecule drugs and nanomaterials on the relationship between macrophage polarization and autophagy may be attributed to their difference in physical and chemical properties.

Taken together, our above data suggest a mechanism underlying PEG-AuNPs induced antitumor immunotherapy, including

inhibiting TAMs M2 polarization *via* induction of lysosome dysfunction and autophagic flux inhibition (Fig. 8). Upon PEG-AuNPs internalization, the autophagic flux of TAMs was blocked due to lysosomal dysfunction, as reflected by autophagosome accumulation, lysosomal alkalization, and lysosomal membrane permeabilization, following which M2 polarization of TAMs was inhibited, resulting in potential antitumor immunotherapy.

4. Conclusions

Regulation of TAMs polarization emerges as a new promising strategy for tumor immunotherapy. Herein, we successfully initiated antitumor immunotherapy by inhibiting TAMs M2 polarization *via* autophagy intervention with polyethylene glycol-conjugated AuNPs (PEG-AuNPs). Our results suggest a mechanism underlying PEG-AuNPs-induced inhibition on M2 polarization, that PEG-AuNPs can induce lysosome dysfunction and autophagic flux inhibition. This study also showed the intrinsic effect of AuNPs on the tumor microenvironment, which strengthens our in-depth understanding of the interaction of

nanomaterials and tumor microenvironments and may provide strategies for the nanomaterials-guided antitumor therapy.

Author contributions

Siyue Zhang, conceptualization, data curation, and methodology; Fangyuan Xie, formal analysis, writing draft and funding acquisition; Kaichun Li, investigation; He Zhang, visualization and software; You Yin, methodology; Yuan Yu, resources; Guangzhao Lu, methodology; Shihao Zhang, formal analysis; Yan Wei, investigation; Ke Xu, Visualization; Yan Wu, supervision; Hong Jin, software; Lan Xiao, visualization; Leilei Bao, supervision; Can Xu, supervision, writing and editing; Yulin Li, supervision, writing and editing; Ying Lu, supervision and conceptualization; Jie Gao, project administration, writing review, editing, and funding acquisition.

Conflicts of interest

The authors declare no conflict of interest.

Appendix A.   Supporting information

Supporting data to this article can be found online at https://doi.org/10.1016/j.apsb.2022.02.008.

References

1. Arneth B. Tumor microenvironment. *Medicina* 2020;**56**: 15−1.
2. Wu T, Dai Y. Tumor microenvironment and therapeutic response. *Cancer Lett* 2017;**387**:61−8.
3. Zhang SY, Song XY, Li Y, Ye LL, Zhou Q, Yang WB. Tumor-associated macrophages: a promising target for a cancer immunotherapeutic strategy. *Pharmacol Res* 2020;**161**:105−11.
4. Salmaninejad A, Valilou SF, Soltani A, Ahmadi S, Abarghan YJ, Rosengren RJ, et al. Tumor-associated macrophages: role in cancer development and therapeutic implications. *Cell Oncol* 2019;**42**: 591−608.
5. Lin YX, Xu JX, Lan HY. Tumor-associated macrophages in tumor metastasis: biological roles and clinical therapeutic applications. *J Hematol Oncol* 2019;**12**:76.
6. Zhou Q, Xian M, Xiang SF, Xiang DY, Shao XG, Wang JC, et al. All-trans retinoic acid prevents osteosarcoma metastasis by inhibiting M2 polarization of tumor-associated macrophages. *Cancer Immunol Res* 2017;**5**:547−59.
7. Yao ZT, Zhang JQ, Zhang B, Liang GK, Chen X, Yao FQ, et al. Imatinib prevents lung cancer metastasis by inhibiting M2 polarization of macrophages. *Pharmacol Res* 2018;**133**:121−31.
8. Shao XJ, Xiang SF, Chen YQ, Zhang N, Cao J, Zhu H, et al. Inhibition of M2 macrophages by all-trans retinoic acid prevents cancer initiation and stemness in osteosarcoma cells. *Acta Pharmacol Sin* 2019;**40**:1343−50.
9. Huang YJ, Yang CK, Wei PL, Huynh TT, Whang-Peng J, Meng T, et al. Ovatodiolide suppresses colon tumorigenesis and prevents polarization of M2 tumor-associated macrophages through YAP oncogenic pathways. *J Hematol Oncol* 2017;**10**:60.
10. Abd Elkodous M, El-Sayyad G, Abdelrahman I, El-Bastawisy HS, Mohamed AE, Mosallam FM, et al. Therapeutic and diagnostic potential of nanomaterials for enhanced biomedical applications. *Colloids Surf B Biointerfaces* 2019;**180**:411−28.
11. Cheng LC, Jiang XM, Wang J, Chen CY, Liu RS. Nano-bio effects: interaction of nanomaterials with cells. *Nanoscale* 2013;**5**:3547−69.
12. Ovais M, Guo MY, Chen CY. Tailoring nanomaterials for targeting tumor-associated macrophages. *Adv Mater* 2019;**31**:1808303.
13. Singh Y, Pawar VK, Meher JG, Raval K, Kumar A, Shrivastava R, et al. Targeting tumor-associated macrophages (TAMs) *via* nanocarriers. *J Contr Release* 2017;**254**:92−106.
14. Zanganeh S, Hutter G, Spitler R, Lenkov O, Mahmoudi M, Shaw A, et al. Iron oxide nanoparticles inhibit tumour growth by inducing pro-inflammatory macrophage polarization in tumour tissues. *Nat Nanotechnol* 2016;**11**:986−94.
15. MacParland SA, Tsoi KM, Ouyang B, Ma XZ, Manuel J, Fawaz A, et al. Phenotype determines nanoparticle uptake by human macrophages from liver and blood. *ACS Nano* 2017;**11**:2428−43.
16. Hoppstädter J, Seif M, Dembek A, Cavelius C, Huwer H, Kraegeloh A, et al. M2 polarization enhances silica nanoparticle uptake by macrophages. *Front Pharmacol* 2015;**6**:00055.
17. Pal R, Chakraborty B, Nath A, Singh LM, Ali M, Rahman DS, et al. Noble metal nanoparticle-induced oxidative stress modulates tumor-associated macrophages (TAMs) from an M2 to M1 phenotype: an *in vitro* approach. *Int Immunopharm* 2016;**38**:332−41.
18. Levy J, Towers CG, Thorburn A. Targeting autophagy in cancer. *Nat Rev Cancer* 2017;**17**:528−42.
19. Chen PW, Cescon M, Bonaldo P. Autophagy-mediated regulation of macrophages and its applications for cancer. *Autophagy* 2014;**10**: 192−200.
20. Oelschlaegel D, Weiss Sadan T, Salpeter S, Krug S, Blum G, Schmitz W, et al. Cathepsin inhibition modulates metabolism and polarization of tumor-associated macrophages. *Cancers* 2020;**12**:2579.
21. Yang M, Liu JW, Shao JH, Qin YW, Ji QS, Zhang XL, et al. Cathepsin S-mediated autophagic flux in tumor-associated macrophages accelerate tumor development by promoting M2 polarization. *Mol Cancer* 2014;**13**:43.
22. Zhang Q, Li YN, Miao CY, Wang YQ, Xu Y, Dong RF, et al. Anti-angiogenesis effect of neferine *via* regulating autophagy and polarization of tumor-associated macrophages in high-grade serous ovarian carcinoma. *Cancer Lett* 2018;**432**:144−55.
23. Tan HY, Wang N, Man K, Tsao SW, Che CM, Feng Y. Autophagy-induced RelB/p52 activation mediates tumour-associated macrophage repolarisation and suppression of hepatocellular carcinoma by natural compound baicalin. *Cell Death Dis* 2015;**6**:e1942.
24. Zabirnyk O, Yezhelyev M, Seleverstov O. Nanoparticles as a novel class of autophagy activators. *Autophagy* 2007;**3**:278−81.
25. Gao J, Chen XH, Ma TJ, He B, Li P, Zhao YC, et al. PEG-ceramide nanomicelles induce autophagy and degrade tau proteins in N2a cells. *Int J Nanomed* 2020;**15**:6779−89.
26. Mei L, Zhang XD, Feng SS. Autophagy inhibition strategy for advanced nanomedicine. *Nanomedicine* 2014;**9**:377−80.
27. Yang KX, Lu Y, Xie FY, Zou H, Fan XY, Li BH, et al. Cationic liposomes induce cell necrosis through lysosomal dysfunction and late-stage autophagic flux inhibition. *Nanomedicine* 2016;**11**:3117−37.
28. Guo LL, He NY, Zhao YX, Liu TH, Deng Y. Autophagy modulated by inorganic nanomaterials. *Theranostics* 2020;**10**:3206−22.
29. Halamoda Kenzaoui B, Chapuis Bernasconi C, Guney-Ayra S, Juillerat-Jeanneret L. Induction of oxidative stress, lysosome activation and autophagy by nanoparticles in human brain-derived endothelial cells. *Biochem J* 2012;**441**:813−21.

30. Scherz-Shouval R, Elazar Z. Regulation of autophagy by ROS: physiology and pathology. *Trends Biochem Sci* 2011;**36**:30−8.

31. Li JJ, Hartono D, Ong CN, Bay BH, Yung LYL. Autophagy and oxidative stress associated with gold nanoparticles. *Biomaterials* 2010;**31**:5996−6003.

32. Zhang XJ, Chen S, Huang KX, Le WD. Why should autophagic flux be assessed? *Acta Pharmacol Sin* 2013;**34**:595−9.

33. Stern ST, Adiseshaiah PP, Crist RM. Autophagy and lysosomal dysfunction as emerging mechanisms of nanomaterial toxicity. *Part Fibre Toxicol* 2012;**9**:20.

34. Link S, El-Sayed MA. Size and temperature dependence of the plasmon absorption of colloidal gold nanoparticles. *J Phys Chem B* 1999;**103**:4212−7.

35. Xu YY, Wang LM, Bai R, Zhang TL, Chen CY. Silver nanoparticles impede phorbol myristate acetate-induced monocyte-macrophage differentiation and autophagy. *Nanoscale* 2015;**7**:16100−9.

36. Kang MS, Lee SY, Kim KS, Han DW. State of the art biocompatible gold nanoparticles for cancer theragnosis. *Pharmaceutics* 2020;**12**:701.

37. Eck W, Craig G, Sigdel A, et al. Pegylated gold nanoparticles conjugated to monoclonal F19 antibodies as targeted labeling agents for human pancreatic carcinoma tissue. *ACS Nano* 2008;**2**:2263−72.

38. Miao XY, Leng XF, Zhang Q. The current state of nanoparticle-induced macrophage polarization and reprogramming research. *Int J Mol Sci* 2017;**18**:336.

39. Huang KY, Ma HL, Liu J, Huo SD, Kumar A, Wei T, et al. Size-dependent localization and penetration of ultrasmall gold nanoparticles in cancer cells, multicellular spheroids, and tumors *in vivo*. *ACS Nano* 2012;**6**:4483−93.

40. Wang XY, Cui XG, Zhao YL, Chen CY. Nano-bio interactions: the implication of size-dependent biological effects of nanomaterials. *Sci China Life Sci* 2020;**63**:1168−82.

41. Kuang DM, Wu Y, Chen NN, Cheng JS, Zhuang SM, Zheng LM. Tumor-derived hyaluronan induces formation of immunosuppressive macrophages through transient early activation of monocytes. *Blood* 2007;**110**:587−95.

42. Wang QS, Ni H, Lan L, Wei XL, Xiang R, Wang Y. Fra-1 proto-oncogene regulates IL-6 expression in macrophages and promotes the generation of M2d macrophages. *Cell Res* 2010;**20**:701−12.

43. Li YJ, Guo WW, Su XD, Ou-Yang L, Dang M, Tao J, et al. Small size mesoporous organosilica nanorods with different aspect ratios: synthesis and cellular uptake. *J Colloid Interface Sci* 2018;**512**:134−40.

44. Gao HJ, Shi WD, Freund LB. Mechanics of receptor-mediated endocytosis. *Proc Natl Acad Sci U S A* 2005;**102**:9469−74.

45. Egami Y. Molecular imaging analysis of Rab GTPases in the regulation of phagocytosis and macropinocytosis. *Anat Sci Int* 2016;**91**:35−42.

46. Costa Verdera H, Gitz-Francois JJ, Schiffelers RM, Vader P. Cellular uptake of extracellular vesicles is mediated by clathrin-independent endocytosis and macropinocytosis. *J Contr Release* 2017;**28**:100−8.

47. Barrias ES, Reignault LC, Souza WD, Carvalho T. Dynasore, a dynamin inhibitor, inhibits trypanosoma cruzi entry into peritoneal macrophages. *PLoS One* 2010;**5**:e7764.

48. Liu JY, Geng XF, Hou JX, Wu GS. New insights into M1/M2 macrophages: key modulators in cancer progression. *Cancer Cell Int* 2021;**21**:389.

49. Deng ZY, Sun MM, Wu J, Fang HH, Cai SM, An S, et al. SIRT1 attenuates sepsis-induced acute kidney injury *via* beclin1 deacetylation-mediated autophagy activation. *Cell Death Dis* 2021;**12**:217.

50. Huang Z, Yang Y, Jiang YC, Shao J, Sun XL, Chen JN, et al. Antitumor immune responses of tumor-associated macrophages *via* toll-like receptor 4 triggered by cationic polymers. *Biomaterials* 2013;**34**:746−55.

51. Li YB, Ju DW. The role of autophagy in nanoparticles-induced toxicity and its related cellular and molecular mechanisms. *Adv Exp Med Biol* 2018;**1048**:71−84.

52. Jiang PD, Mizushima N. LC3- and p62-based biochemical methods for the analysis of autophagy progression in mammalian cells. *Methods* 2015;**75**:13−8.

53. Mizushima N, Levine B, Cuervo AM, Klionsky DJ. Autophagy fights disease through cellular self-digestion. *Nature* 2008;**451**:1069−75.

54. Anwar T, Liu XN, Suntio T, Marjamäki A, Biazik J, Chan EYW, et al. ER-targeted beclin 1 supports autophagosome biogenesis in the absence of ULK1 and ULK2 kinases. *Cells* 2019;**8**:475.

55. Chang CP, Su YC, Hu CW, Lei HY. TLR2-dependent selective autophagy regulates NF-kB lysosomal degradation in hepatoma-derived M2 macrophage differentiation. *Cell Death Differ* 2013;**20**:515−23.

56. Liu PH, Huang GJ, Wei T, Gao J, Huang CL, Sun MW. Sirtuin 3-induced macrophage autophagy in regulating NLRP3 inflammasome activation. *Biochim Biophys Acta Mol Basis Dis* 2018;**1864**:764−77.

57. Nakahira K, Haspel J, Rathinam V, et al. Autophagy proteins regulate innate immune responses by inhibiting the release of mitochondrial DNA mediated by the NALP3 inflammasome. *Nat Immunol* 2011;**12**:222−30.

58. Chen D, Xie J, Fiskesund R, Dong W, Liang X, Lv J, et al. Chloroquine modulates antitumor immune response by resetting tumor-associated macrophages toward M1 phenotype. *Nat Commun* 2018;**9**:873.